

MIT Open Access Articles

*Particle laden flows through an inverted chimney
with applications to ocean carbon sequestration*

The MIT Faculty has made this article openly available. **Please share**
how this access benefits you. Your story matters.

Citation: Chow, Aaron C., and E. Eric Adams. "Particle Laden Flows through an Inverted Chimney with Applications to Ocean Carbon Sequestration." *Environ Fluid Mech* 12, no. 1 (February 2012): 3–21.

As Published: <http://dx.doi.org/10.1007/s10652-010-9200-1>

Publisher: Springer-Verlag

Persistent URL: <http://hdl.handle.net/1721.1/85662>

Version: Author's final manuscript: final author's manuscript post peer review, without publisher's formatting or copy editing

Terms of Use: Article is made available in accordance with the publisher's policy and may be subject to US copyright law. Please refer to the publisher's site for terms of use.



Particle laden flows through an inverted chimney with applications to ocean carbon sequestration

Aaron C. Chow¹, E. Eric Adams²

¹Gnarus Advisors, LLC, 470 Totten Pond Rd., Suite 501, Waltham, MA 02451, USA.

²Department of Civil and Environmental Engineering, Massachusetts Institute of Technology, Room 48-216b, 15 Vassar St., Cambridge, MA 02139, USA.

ABSTRACT

Plumes of negatively buoyant hydrate particles, formed by reacting liquid CO₂ with seawater at ocean depths of 1000 to 1500 m, have been suggested as a way to help sequester CO₂. The vertical flux of CO₂ can be increased by constructing a shroud around the hydrate particle source to shelter the plume from effects of ambient stratification and current. The shroud also serves as an inverted chimney, inducing a down draft that will transport the dissolving particles to a depth of lower ambient disturbance. Laboratory PIV measurements are compared to an analysis of an idealized shroud that is long, frictionless and driven by a single phase source of buoyancy distributed uniformly over the shroud base. Results indicate that induced draft, and hence dilution of dissolved CO₂, increases with plume buoyancy, and shroud length and diameter, but efficiency decreases with increasing ratio of particle slip velocity divided by the characteristic induced draft velocity. While larger particles show reduced plume-like behavior and hence are less efficient in inducing draft, they still generated about half of the theoretically predicted flow.

Keywords: Ocean carbon sequestration, chimney, shroud, ducted flow, draft, PIV, hydrates, buoyant plumes.

INTRODUCTION

Our study was motivated by several field experiments in which solid CO₂ hydrate particles were injected into the ocean at depths of 1000 to 1500 m. The experiments were designed to help assess the effectiveness of hydrates for sequestering anthropogenic CO₂. Rising concentrations of greenhouse gases in the atmosphere are implicated in adverse climate changes, and two-thirds of the change is attributed to CO₂ [1]. CO₂ hydrates consist of molecules of CO₂ inside a cage-like structure of hydrogen bonded water molecules [2]. They are of interest as a possible vehicle for deeper ocean carbon sequestration, because they are denser than seawater, and will sink unaided while dissolving to promote dispersion in the ocean.

Pure hydrate particles are difficult to produce, but the Oak Ridge National Laboratory (ORNL) has designed a continuous CO₂-seawater co-flowing injector to create cylindrical *composite* particles comprised of CO₂ hydrate (negatively buoyant), liquid CO₂ (slightly positively buoyant at 1000-1500 m depths) and seawater [3]. Field tests were conducted on three occasions using different injectors in collaboration with the Monterey Bay Aquarium Research Institute (MBARI) [4-7]. The latest survey, with a hydrate reactor located at an ocean depth of ~1500 m, produced curved negatively buoyant cylindrical particles with diameters ~2.2 cm and lengths up to ~1 m.

Applying a drag coefficient model [8, and Chow and Adams, submitted to *J. Hydraul. Eng.*, 2010] to observed initial settling velocities and dissolution rates during the most recent survey, we concluded that the hydrate conversion efficiency (percentage of liquid CO₂ converted to hydrate) in the field was ~ 15-20% resulting in particles with specific gravity 1-2% greater than seawater, which lead them to sink to a depth below discharge of roughly 100 m. Greater sinking could obviously be achieved using larger particles. Discharging particles with a range of sizes and densities (reflecting different conversion rates) would cause differential settling resulting in spreading in the down-current and vertical directions. Furthermore, towing the source from a moving ship

would contribute additional dispersion. Such strategies, and associated environmental impacts, are discussed in [9].

An alternative approach to enhancing mixing and vertical descent is to release a continuous stream of particles, forming a dense plume which would sink both due to the density of the particles as well as the increased density of seawater containing dissolved CO₂. An integral double plume model [10 – 12] was used to simulate the behavior of continuous streams of composite particles released to a quiescent ocean, with typical ambient stratification, at CO₂ loadings of 0.01 to 1000 kg/s. Results showed that, for a CO₂ release of 100 kg/s (roughly the emission from a 500 MW coal-fired power plant), a plume composed of 2.2 cm diameter composite particles with 16% reaction efficiency would sink about 1000 m, approximately 10 times the individual particle sinking depth. A plume composed of similar particles, but with a diameter of 5 cm, would sink about 2000 m (~5 times the individual particle depth), while plumes composed of larger particles, or particles exhibiting higher reaction efficiency, would reach the seafloor (as would the individual particles).

However, two ambient effects reduce the performance of a plume: stratification and ocean currents. Plume sinking is hampered by strong ambient stratification which causes trapping of entrained seawater at intermediate depths below release. Density stratification weakens at depths below 1500 m [13], so from the perspective of reduction of plume trapping, the deeper regions of the ocean are potentially favorable for depositing CO₂.

More importantly, ambient ocean currents are known to cause a different type of phase separation, whereby the continuous fluid in the plume is swept downstream of the particles which sink more directly. Typical ocean currents range from 0-40 cm/s and are more variable with depth and global position than ambient densities [13]. A CO₂ hydrate plume released in the presence of a current is prone to plume separations [14], and in a typical current will result in lower dilution and sinking depths. This paper discusses the possible use of a shroud that could prevent such separations.

SHROUDED FLOWS

Concept

Figure 1 shows a schematic of a fixed shroud, or inverted chimney that could be constructed around a plume release in order to reduce the two ambient effects. The shroud extends a length h below the plume release and has diameter d . As the particles are released into the shroud, they induce a down draft composed of ambient seawater entrained at the top of the shroud. Releasing particles into a stationary shroud will therefore negate the effects of an ambient current and density stratification, delivering the sinking particles to their intended depth.

Examples of Ducted flows

Shrouds, ducts and chimneys have often been suggested as ways to promote dilution and transport. Silvester [15] and Argaman et al. [16] studied a submerged axisymmetric sewage discharge in shallow water and suggested that a shroud around the discharge would set up a pressure gradient and would lengthen the plume trajectory, increasing horizontal momentum and dilution of the effluent. The situation is akin to a water jet pump and results in enhanced dilution compared with a free jet especially if the entrance loss is reduced by building a flared opening. Adams [17] and Parr and Melville [18] studied uni-directional multi-port jet diffusers used in shallow water to dilute thermal discharges from electric power plants. They found that dilution was limited by the contraction of the jets as they merged and that such contraction could be eliminated by erecting a channel around the nozzles. Buoyant chimneys and natural draft cooling towers set up a pressure gradient to induce a vertical draft, either for drawing in oxygen to sustain a fire or to remove latent heat [19]. Air lift pumps are commonly used to induce an upward flow using a highly buoyant second phase [20]. Kajishima et al. [21] and Adams et al. [22] have considered such concepts to dissolve CO₂ for ocean carbon sequestration: injected CO₂ bubbles or buoyant droplets initially rise in a submerged pipe (or tank), but the heavier CO₂ enriched seawater induces a down draft leading to sinking.

Ideal shroud

Our hydrate release creates a buoyancy-induced, downward flow that is to be shielded from ambient effects using a shroud. We first consider an ideal case where a single phase, negatively buoyant source is distributed uniformly across the top of a frictionless shroud. As shown in the right hand panel of Figure 1, the shroud is a wide fixed vertical pipe with constant diameter d , cross sectional area A , and height h below the release. A Bernoulli equation for flow along a streamline entering the shroud yields

$$\frac{\Delta p}{\rho_w g} = \frac{1}{2} \frac{u^2}{g(1+K)} \quad (1)$$

where $u = Q/A$ is the mean induced velocity, ρ_w is the ambient fluid density, g is gravity, Δp is the pressure difference between the inside and outside of the bottom of the shroud, Q is the flow rate induced by the shroud, and K is an entrance loss coefficient for the shroud. Mays [23] discusses entrance losses for a range of fittings and valves. For example, $K=1$ for a reentrant orifice (e.g. a Borda mouthpiece) and $K \sim 0$ for a flared entrance.

The pressure difference driving the flow (Δp in the LHS of Equation 1) can be taken as the excess weight per unit area of the column of denser fluid (density difference $\Delta\rho$) within the shroud:

$$\Delta p = \frac{1}{A} \int_0^h \Delta\rho g A dz (1+K) = \Delta\rho g h \quad (2)$$

Substituting Equation 2 into Equation 1, and using $B = (\Delta\rho/\rho_w)gQ$ for the kinematic buoyancy flux,

$$\frac{\Delta\rho g h}{\rho_w g} = \frac{1}{2} \frac{u^2}{g(1+K)} \quad (3)$$

$$\frac{Bh}{Q} = \frac{1}{2} \frac{Q^2}{A^2} (1+K) \quad (4)$$

which yields the expression for the induced flow rate:

$$Q = \left(\frac{2BA^2h}{1+K} \right)^{1/3} \quad (5)$$

For a straight shroud opening the entrance loss coefficient can be taken as $K=1$, yielding a relation for the theoretical shroud induced flow $Q=Q_{\text{theo}}$:

$$Q_{\text{theo}} = (BA^2h)^{1/3} \quad (6)$$

Equation 6 is only valid for shroud aspect ratios h/d large enough to prevent upward intrusion of ambient water at the shroud bottom. A criterion for “full flow” exiting the shroud is that the exit densimetric Froude number be greater than about one [24] which leads to a theoretical criterion being $h/d > 1$, though in practice a narrower shroud would be called for. Equation 6 shows that the shroud induced draft increases with cross sectional area and shroud length, i.e. a wider and taller shroud will induce more flow.

Comparison with free plume

A free (unshrouded) plume of the same buoyancy, released from a point in a quiescent unstratified ambient will have a flow rate at the depth of the shroud exit in the following form [25]:

$$Q_{\text{free}} = 0.15B^{1/3}z^{5/3} \quad (7)$$

Taking the ratio of the free plume flow rate and the induced flow from a theoretical chimney,

$$\frac{Q_{\text{free}}}{Q_{\text{theo}}} = \frac{0.15B^{1/3}z^{5/3}}{B^{1/3}A^{2/3}h^{1/3}} = \frac{0.15z^{5/3}}{\left(\frac{\pi}{4}d^2\right)^{2/3}h^{1/3}} = 0.18\left(\frac{h}{d}\right)^{\frac{4}{3}}\left(\frac{z}{h}\right)^{\frac{5}{3}} \quad (8)$$

The outlet plume flow rate for both cases is given at $z = h$

$$\left. \frac{Q_{\text{free}}}{Q_{\text{theo}}} \right|_{z=h} = 0.18\left(\frac{h}{d}\right)^{\frac{4}{3}} \quad (9)$$

Solving for $Q_{\text{free}}/Q_{\text{theo}}=1$, the idealized flow for a chimney induced draft Q_{theo} exceeds that of a free plume where the aspect ratio h/d less than about 3.7. We note that for $1 < h/d < 3.7$, the theoretical flow induced by a ducted buoyancy source exceeds that of a free plume with the same buoyancy. The increased flow results from suction at the top of the

shroud – the same mechanism underlying the ducted flows from single and multiple port outfalls as discussed above. A plot with theoretical induced flow normalized by Q_{theo} is shown in Figure 2.

Effect of central buoyancy source

The flow predicted by Equation 6 applies to a buoyancy source that is distributed evenly across the top of the chimney. In scenarios where the buoyancy source is released from a central port, as envisioned here, the suction near the top of the chimney is less than in the ideal case as the plume itself has not yet spread over the cross section.

Observations of single phase turbulent plumes show that the top hat plume width increases linearly with vertical distance, with a proportionality constant of about 0.2. Using the approach of Equation 2, the pressure difference at the top of the shroud now becomes

$$\Delta p = \frac{1}{A} \int \Delta \rho g A dz = \frac{g}{A} \int \Delta \rho_{\text{plume}} A_{\text{plume}} dz + \frac{g}{A} \int \Delta \rho_w (A - A_{\text{plume}}) dz \quad (10)$$

Since the density difference of the water is $\Delta \rho_w = 0$, Equation 10 becomes

$$\Delta p = \frac{g}{A} \int \Delta \rho_{\text{plume}} A_{\text{plume}} dz \quad (11)$$

From here let $\Delta \rho = \Delta \rho_{\text{plume}}$. The growth of the cross sectional area of the plume within the shroud is described by

$$A_{\text{plume}} = \begin{cases} A \left(\frac{0.2z}{d} \right)^2 & 0.2z < d \\ A & 0.2z \geq d \end{cases} \quad (12)$$

The entrance pressure difference is therefore

Case $0.2h < d$ (or $h/d < 5$)

$$\Delta p = \frac{g}{A} \int_0^h \Delta \rho A \left(\frac{0.2z}{d} \right)^2 dz = \Delta \rho g \left(\frac{0.2h}{d} \right)^2 \frac{h}{3}$$

Case $0.2h \geq d$ (or $h/d \geq 5$)

$$\Delta p = \frac{g}{A} \int_0^{\frac{d}{0.2}} \Delta \rho A \left(\frac{0.2z}{d} \right)^2 dz + \frac{g}{A} \int_{\frac{d}{0.2}}^h \Delta \rho A dz = \Delta \rho g \left(h - \frac{d}{0.6} \right) \quad (13)$$

Substituting both cases into Equation 1:

Case $0.2h < d$ (or $h/d < 5$)

$$\frac{\Delta \rho g \left(\frac{0.2h}{d} \right)^2 \frac{h}{3}}{\rho g} = \frac{1}{2} \frac{u^2}{g(1+K)}$$

$$2BA^2 \left(\frac{0.2h}{d} \right)^2 \frac{h}{3} = Q^3(1+K)$$

Case $0.2h \geq d$ (or $h/d \geq 5$)

$$\frac{\Delta \rho g \left(h - \frac{d}{0.6} \right)}{\rho g} = \frac{1}{2} \frac{u^2}{g(1+K)}$$

$$2BA^2 \left(h - \frac{d}{0.6} \right) = Q^3(1+K) \quad (14)$$

Normalizing the two new predicted flows (Equation 14) by Q_{theo} , using $K=1$, results in the efficiency of the shroud with a central buoyancy source, Q_c/Q_{theo} , as a function of aspect ratio:

$$\frac{Q_c}{Q_{\text{theo}}} = \frac{Q_c}{(BA^2h)^{1/3}} = \begin{cases} \left(\frac{1}{3} \left(\frac{0.2h}{d} \right)^2 \right)^{\frac{1}{3}} & \frac{h}{d} < 5 \\ \left(1 - \frac{2}{3} \frac{1}{0.2} \frac{d}{h} \right)^{\frac{1}{3}} & \frac{h}{d} \geq 5 \end{cases} \quad (15)$$

Figure 2 plots shroud efficiency (expressed by normalized Q_c) as a function of aspect ratio, for a plume released from a central source. Since at aspect ratios lower than about 5, we do not expect the plume to fill the shroud cross section, the flow is more likely to behave like a free plume (as discussed above). Moreover, the confinement of the shroud near the top may cause Coanda effects whereby the plume interacts with the shroud forming a "wall plume". This non-ideal behavior suggests that both Q_{free} and Q_{theo} are upper bounds for the flow induced at the respective ranges of h/d .

Effect of pipe friction

In a real shrouded plume release scenario, the flow through the shroud interior is subjected to pipe friction that increases with the shroud height. A Darcy-Weisbach friction factor f is commonly used to define head loss in a pipe (shroud) as

$$h_{pipe} = f \frac{h}{d} \frac{u_{shroud}^2}{g} \quad (16)$$

Incorporating the effect of friction, the formulation of the pressure head balance (Equation 1) becomes

$$\frac{\Delta p}{\rho_w g} = \frac{1}{2} \frac{u_{shroud}^2}{g} \left(1 + K + f \frac{h}{d} \right) \quad (17)$$

A value for f can be determined from a Moody diagram based on the Reynolds number Re and relative roughness. The Reynolds number of the induced flow based on the shroud diameter and Q_{theo} ranges from 5000-10000. Using an effective relative roughness range of 10^{-6} (essentially smooth) to 0.02 (a conservatively high value: 2% of the shroud diameter) for this range of Re , f will vary from 0.03 (for smooth full flow) to 0.055 [23].

With pipe friction the induced draft (distributed single phase buoyancy source), denoted Q_f , becomes:

$$Q_f = \left(\frac{1 + K}{1 + K + f \frac{h}{d}} BA^2 h \right)^{1/3} \quad (18)$$

Taking the ratio of the prediction of the induced draft with and without friction yields

$$\frac{Q_f}{Q_{theo}} = \left(\frac{1 + K}{1 + K + f \frac{h}{d}} \right)^{1/3} \quad (19)$$

Note that the ratio given by Equation 19 can apply to either a distributed plume source, using Q_{free} from Equation 6, or a central plume source by replacing Q_{theo} by Q_c from Equation 15. Figure 2 illustrates the reduction in chimney (shroud) efficiency with increasing friction.

Effects of a dispersed phase source of buoyancy: plume spread and plume formation

Instead of a single (continuous) phase source of buoyancy, our release scenario involves a negatively buoyant solid phase (CO_2 hydrate particles). Thus, in addition to shroud height h , shroud diameter d , and initial kinematic buoyancy B , we expect the induced flow Q_λ to also depend on the particle slip velocity u_s which embodies particle characteristics (density, diameter, shape and inter-particle separation distance). From dimensional analysis we can thus expect:

$$\frac{Q_\lambda}{Q_{theo}} = f\left(\frac{h}{d}, \frac{u_s}{u_{theo}}\right) \quad (20)$$

where the theoretical induced draft is given by $Q_{theo} = (BA^2h)^{\frac{1}{3}}$, where $A = \pi d^2/4$ is the shroud cross sectional area and u_{theo} is the theoretical mean shroud induced fluid velocity, equal to Q_{theo}/A . In the limit of small u_s/u_{theo} the flow is expected to behave like that generated by a continuous phase buoyancy source.

One consequence of increased slip velocity on a plume is the effect on plume spreading. Previous discussion pertains to a single, continuous phase, source of buoyancy leading to plumes of well defined width. However, as has been observed by Milgram [26] and Asaeda and Imberger [27], particles (or bubbles) produce a multi-phase plume that only occupies a central core which is smaller than the liquid portion of the plume. For bubble plumes, Socolofsky and Adams [14] obtained a relation between the plume spreading ratio (width of bubbles versus total plume width, λ) as a function of the bubble characteristics, by measuring the edge of the inner particle core with a dyed edge of the plume fluid. They found

$$\lambda = 1 - 0.19U_N^{0.61} \quad (21)$$

where $U_N = u_s / (BN)^{\frac{1}{4}}$ is the slip velocity, normalized by a characteristic plume speed in stratification. We can use a similar non-dimensional slip velocity, this time in the following form:

$$\frac{u_s}{u_{theo}} = \frac{u_s}{Q_{theo}/A} = \frac{u_s}{(Bh/A)^{1/3}} \quad (22)$$

The plume spreading ratio is taken into account in the predictions by replacing 0.2 with 0.2λ in Equation 15 to give

$$\frac{Q_\lambda}{Q_{theo}} = \frac{Q_\lambda}{(BA^2h)^{1/3}} = \begin{cases} \left(\frac{1}{3} \left(\frac{0.2\lambda h}{d} \right)^2 \right)^{1/3} & \frac{h}{d} < \frac{1}{0.2\lambda} \\ \left(1 - \frac{2}{3} \frac{1}{0.2\lambda} \frac{d}{h} \right)^{1/3} & \frac{h}{d} \geq \frac{1}{0.2\lambda} \end{cases} \quad (23)$$

where we adapt Equation 21 for the plume spreading ratio

$$\lambda = 1 - 0.19 \left(\frac{u_s}{u_{theo}} \right)^{0.61}. \quad (24)$$

u_s/u_{theo} values for our experiments ranged from 0 to ~3.8, resulting in λ values of about 0.57 to 1 using Equation 24. Figure 2 shows the reduction of the shroud efficiency as a result of both friction and a reduced plume spreading rate corresponding to $\lambda=0.5$.

Onset of plume behavior

The term u_s/u_{theo} in Equation 20 also relates to how groups of particles interact with each other to form a plume. The numerical plume descent depth predictions from Chow [8] and the theoretical analysis presented herein assume that the resulting release will behave as a turbulent plume, regardless of particle number frequency and size.

Interactions between different particles have been studied for the purpose of understanding the dynamics of bubble coalescence and breakup due to collisions. Among the studies, observations have been made for pairs of bubbles [17], chains of bubbles [28], groups of bubbles [29] and bubble swarms [30, 31]. Tsuchiya et al. [29], in experiments performed in a 2D cell simulating a fluidized bed, investigated air bubbles ($Re = 2000-13000$) to determine behavior between bubbles and wakes. They found that if a trailing bubble is within about 5-7 bubble diameters of the leading bubble, it will catch up (due to low pressure in the leading bubble's wake) and cause bubble pairing side by side, or coalescence. Lazarek and Littman [32] measured the pressure field around a

single spherical capped air bubble in water ($Re=26700$) and showed that there is a pressure minimum directly behind the bubble at about 2 bubble diameters downstream.

Table 1 shows that a design release of 100 kg/s of CO_2 , using the particles observed during the most recent field survey [6], requires a particle release rate of ~5300 particles per second. Larger particles, and or particles with higher hydrate conversion efficiency, require smaller particle release rates (as low as 250 particles per second as indicated in Table 1). The number release rate can be translated to an estimated particle spacing (assuming that particles remain in single file after release) by dividing the particle number rate by the slip velocity. The particle spacing varies from 0.0003 to 0.01 particle diameters, all significantly less than 1, meaning that the particles interact with each other, and must spread laterally prior to descending, and supports the assumption of plume formation. However, it is possible that particles would no longer form a plume in hydrate particle release scenarios using particles with greater density and size from a reactor that is further scaled up. In addition, experimental simulations (described below) designed to simulate the plumes may use particle releases with higher particle spacings (greater than one particle diameter) such that a plume would not be formed. For these reasons a study of the effect of particle spacing on plume behavior is included in our analysis.

Table 1. Predicted particle number release rates and particle spacing for typical field and scaled-up field particles attainable with current technology. Refer to Tsouris et al. [6].

Particle name	2006	2006+	2006++	2006+++
Init. diameter d (cm)	2.2	5	10	10
Init. length L (cm)	30	30	30	30
Init. sinking rate (cm/s)	4	6	8	27
ρ (g/cm³)	1.04	1.04	1.04	1.08
Release rate for 100 kg/s CO_2 mass loading (particles/s)	5270	1020	260	250
Expected particle spacing (particle diameters)	0.0003	0.001	0.003	0.011

EXPERIMENTS

Experiments were performed to determine whether a shrouded plume indeed induces a draft, and whether aspect ratio and particle size affect shroud efficiency as discussed in the previous sections.

Experimental Set-up

Experiments were conducted in a 1.22 m by 1.22 m by 2.44 m tall tank in the R. M. Parsons Hydrodynamics Laboratory at the Department of Civil and Environmental Engineering at MIT. Shrouds were constructed of PVC pipes or rigid sheets of plastic rolled into a cylindrical shape. The shrouds ranged in diameter from 7.5 cm to 30 cm and ranged from 30 cm to 157 cm in length ($h/d = 1-21$). The shrouds were suspended in the tank by four strings from the four top corners of the tank. In order to reduce spurious effects from either the water surface or the bottom of the tank, the top of the shroud was always at least 3 diameters from the surface and the bottom of the shroud was at least 3 diameters from the tank bottom.

Buoyancy sources

Six buoyancy sources were used: brine, small glass beads and plastic balls of four different densities (made by filling hollow polystyrene spheres with brine or molasses). The glass beads used were Ballotini impact glass beads, available in various sizes, used industrially for finishing smooth metal surfaces. Table 2 shows the characteristics of the six buoyancy sources. The size distribution of the small glass beads and polystyrene seeding particles were obtained by sieve analysis and their slip velocities calculated by an empirical relation based on a spherical particle by Dietrich [33]. The slip velocity of the balls were obtained by releasing the particles into the tank and measuring the time taken to cross a start and finish line, as described in Chow [8]. Their densities were either calculated by dividing their mass by their volume, or deduced from their observed velocities and applying a spherical drag coefficient. Table 2 also summarizes the polystyrene particles used for PIV measurements.

Table 2. Buoyancy sources and particles used in shroud experiments, with measured particle number release rates \dot{N} .

	ρ	$d(\text{mm})$		$u_s (\text{cm/s})$		Measured \dot{N}
	(kg/m^3)	Mean	Std. dev.	Mean	Std. dev.	(particles/s)
Brine	1100-1360	-	-	-	-	-
Beads	2450	0.15	0.016	1.2	0.2	600000
Ball (LLD)	1010	18.8	0.05	7.8	0.9	2.5
Ball (LD)	1060	18.8	0.05	18.3	2.0	6
Ball (MD)	1070	18.8	0.05	20.8	0.2	4
Ball (HD)	1210	18.8	0.05	33.0	1.9	2
Polystyrene (PIV seeding particles)	1050	0.32	0.027	0.2	0.03	-

The release mechanisms for each buoyant discharge type are illustrated in Figure 3 and described in more detail in Chow [8]. For consistency we sought a constant initial buoyancy flux B among the experiments. Actual initial buoyancy fluxes for the experiments had a mean of $B=1470 \text{ cm}^4/\text{s}^3$, with standard deviation $550 \text{ cm}^4/\text{s}^3$ (37%). Since the measured flow rates are normalized by Q_{theo} which includes B , the variation in B between experiments is not of importance.

Qualitative behavior

Figure 4 shows images of the steady buoyant releases in shrouds of different aspect ratios ($h/d=2, 4$ and 10). Due to the thickness of the transparent PVC of the shroud, the actual plume widths within the shroud cannot be measured quantitatively, but inspection shows that the plume does spread to fill the shroud cross section by about 4 or 5 shroud diameters. The bottom panel of Figure 4 shows that by 10 shroud diameters, brine and bead plumes are fully spread over the shroud cross section.

Conversely, the top panel of Figure 4 for $h/d=2$ shows a plume that has clearly not completely spread over the cross section. Although not discerned in the figure, some releases showed evidence of the Coanda effect, with the plume attaching to one side of the shroud walls at random. The right hand panels of each figure show the release of the

heaviest particles. Although a plume effect is not immediately apparent in these figures, typical particle spacings for the balls shown were about 8.4 diameters, close enough for particles to interact with each other for group behavior, as described previously. As a result, the ball releases do show a significant induced flow.

Particle image velocimetry

Particle Image Velocimetry (PIV) was used to measure the induced flows into the shroud for all particle and brine releases, and is described in more detail in Chow [8]. In order to illuminate a slice of the flow into the shroud, a vertical laser light sheet with thickness of about 0.5 cm was directed radially into the center of the shroud. The laser used was a Coherent Innova 70 Argon-ion laser at 4 Watts continuous output power, attached to an optical fiber with a cylindrical lens affixed at its end that created the light sheet. Polystyrene seeding particles of average diameter 315 microns obtained by sieve analysis (corresponding to slip velocity of 0.17 cm/s using the equation of Dietrich [33]) were used to seed the flow for illumination by the laser (refer to Table 2). A Prosilica EC640 1/2 inch CMOS Firewire camera with 659 x 493 pixel resolution was used for image acquisition. Timestamps of each image were made with each image acquired, and were used to determine the time elapsed between frames. Typically 900 to 2400 images were taken in succession with a frame rate of about 50 frames per second resulting in a velocity record of 18-48 s of the duration for each shroud experiment. MATPIV was used in conjunction with MATLAB to analyze velocities from the images. Gui and Merzkirch [34] discuss different correlation methods used for PIV, and concluded that the minimum quadratic difference (MQD) method is suited for images with non-uniform lighting. Regions of Interest (ROIs) of 64 by 64 pixels were used for the shroud images. For each ROI, the calculated displacements, expressed in pixels, can be converted to an instantaneous velocity using the scale of the image (cm per pixel) and the time elapsed between the two images (s). The total image size of 648 x 485 pixels results in sufficient ROIs available per image to generate a velocity field as shown in Figure 5.

Induced flow determination

The laser illuminated a radial slice of the shroud through its center as shown in Figure 5. Flow rates were determined by analyzing velocities collected at the shroud entrance. (The shroud entrance was used, rather than the exit, due to the lower effect of the high reflectivity particles on the image contrast in the former.) Figure 5 shows the rectangular 2D control volume used to determine the flow entering the shroud. The control volume is bounded by the injection pipe with radius R_0 , and has the same radius as the shroud $R=d/2$, and a height H extending immediately above the shroud. Assuming axisymmetry, the value of Q is determined by integrating the velocities crossing into control volume and around the shroud, i.e.

$$Q = - \left(2\pi \int_{R_0}^R v(r, H) r dr + 2\pi R \int_0^H u(R, z) dz \right) \quad (25)$$

where $v(r, H)$ and $u(R, h)$ are the steady state values of the vertical (positive upward) and horizontal (positive in the r direction) velocities. Multiple control volumes (i.e. different values of H) were used in each experiment to determine Q .

Steady state velocities

Velocity measurements taken over time at a discrete point indicate that the shroud takes some time to set up a steady siphon effect following the initiation of continuous particle release. In addition, there are velocity fluctuations which indicate that the siphon effect is not constant with time, especially when balls were used as the source of buoyancy (Figure 6). The steady state velocities were determined by averaging over periods of time after the initial velocity ramping. For the example in Figure 6, the steady state was attained after ~ 31 s.

In order to verify the accuracy of the PIV velocities, individual particle displacements from selected images were tracked by eye. Additionally, for several experiments, fluorescent dye was introduced at the top of the shroud, and its

concentration measured with a fluorometer at the exit. Flows measured by dye dilution compared favorably with those computed by integrating PIV-measured velocities [8].

RESULTS

Shroud efficiency

The experimental results for the induced shroud flow rates Q as a function of shroud aspect ratio are presented in Figure 7. The plots show that brine (a single phase flow) and beads that resemble a single phase buoyancy source, as indicated by their low normalized slip velocity, behave similarly to the theoretical predictions. However, flows induced by the larger particles are more intermittent in creating an entrainment flow into the shroud, resulting in lower performance compared to the theoretical predictions. As expected from the discussion on plume onset, the larger the slip velocity in relation to the theoretical induced flow velocity, expressed as u_s/u_{theo} , the smaller the induced flow rate efficiency (Figure 8). Furthermore, the large balls in the shroud underperform even compared to the relation described by a two phase plume, as plotted in the line labeled ' $\lambda=0.5$ ' in Figure 7. This suggests that the particle-driven flows are not fully plume-like.

IMPLICATIONS FOR SHROUDED HYDRATE RELEASE IN THE OCEAN

While results presented above show that the flow induced by shrouds of small aspect ratio are somewhat smaller than the theoretical (idealized) values, the flows can still be quite large in absolute terms, as they depend on the shroud cross sectional area A . Figure 9 plots the estimated actual flowrates for a 100 kg/s release of hydrates of density 1.04 g/cm^3 from a centralized source. Table 3 shows values of u_s/u_{theo} for experimental particle releases and for potential field scale hydrate releases, which lie in a comparable range. We envision that the particle releases are made into ballasted, articulated, flexible shrouds that could be suspended from a ship. Such devices have never been built on such

a scale and would require extensive design and testing to overcome challenges in their deployment and operation. From the previous section, only the high density balls showed reduced plume-like behavior. In order for the shrouded plume to show reduced plume behavior at the scale of the '2006+++' hydrate release, the slip velocity of the particles would need to be about 40-50 cm/s as compared with a calculated value of 26 cm/s. We concluded that scaled up hydrate particle releases are most likely to behave like a plume. Despite the reduced plume-like behavior, the induced flow is still predicted to be about 55-60% of the value of Q_{theo} .

The CO_2 of the particles will ultimately dissolve into the dispersed phase. At the bottom of the shroud, assuming that the particles are dissolved, the added dissolved inorganic carbon (DIC) concentration ΔDIC emerging from the bottom of the shroud is determined by

$$\Delta DIC = \frac{\dot{m}}{Q \left(\frac{h}{d}, \frac{u_s}{u_{theo}} \right)} \quad (26)$$

Table 3. Typical values of u_s/u_{theo} for experiments and expected values for shrouded hydrate plumes. Expected hydrate plume characteristics: 100 kg/s CO_2 mass loading, shroud diameter $d=100$ m, height $h=1000$ m. Hydrate particle characteristics are found in Table 1

Buoyancy source	Slip velocity u_s (cm/s)	B (m^4/s^3)	u_{theo} (cm/s)	$\frac{u_s}{u_{theo}}$
Experiments:				
Brine	0	1.5e-5	11	0
Beads	1.2	1.5e-5	11	0.10
Ball (LLD)	7.8	1.0e-6	4.5	1.72
Ball (LD)	18.3	1.1e-5	10.1	1.82
Ball (MD)	20.8	1.0e-5	10.6	1.96
Ball (HD)	33.0	1.5e-5	11	2.99
Hydrate particles:				
2006	4	0.015	12	0.32
2006+	6	0.015	12	0.48
2006++	8	0.015	12	0.64
2006+++	27	0.132	26	1.05

where \dot{m} is the CO_2 mass loading. In addition to DIC, another measure of plume impact is pH which can be determined by the method outlined in Israelsson et al. [9]. DIC was

converted to pCO_2 by solving the carbonate system using dissociation constants from Dickson and Goyet [35] and solubility from Weiss [36]. The following average deep-ocean chemistry was assumed, based on Volk and Hoffert [37]: salinity = 35 ppt, ambient DIC = 2,306 $\mu\text{mol/kg}$, and C-Alk = 2,367 $\mu\text{mol/kg}$. Temperature was set to 3°C , resulting in an ambient pH of about 7.9. For a 100 kg/s CO_2 release into a shroud with diameter of 100 m and height of 1000 m, the predicted added DIC and pH drops are shown in Table 4. It is important to note that the predicted added CO_2 concentrations and resultant pH drops listed in Table 4 are the average values of pH leaving the shroud and that further dilution will occur beyond the exit.

Table 4. Typical dilutions achieved by shrouded hydrate plumes. Expected hydrate plume characteristics: 100 kg/s CO_2 mass loading, shroud diameter $d=100$ m, height $h=1000$ m. Hydrate particle characteristics are found in Table 1. Estimated shroud efficiencies obtained by inspection of the plot in Figure 9.

Hydrate particles	u_s (cm/s)	B (m^4/s^3)	u_{theo} (cm/s)	$\frac{u_s}{u_{\text{theo}}}$	Q_{theo} (m^3/s)	Est. efficiency	Predicted Q (m^3/s)	Added DIC at exit (kg/m^3)	pH drop at exit
2006	4	0.015	12	0.32	980	65%	637	0.16	1.59
2006+	6	0.015	12	0.48	980	60%	588	0.17	1.62
2006++	8	0.015	12	0.64	980	55%	539	0.19	1.66
2006+++	27	0.132	26	1.05	2013	50%	1007	0.10	1.39

CONCLUSIONS

We investigated a strategy of sequestration of CO_2 hydrates by injecting them into a shroud (a tall inverted chimney). The goal of the shroud is to protect the hydrate release from ambient stratification and crossflow currents, and to promote better control of CO_2 plume placement. Predictions based on physical arguments and experimental observations show that a long shroud will induce a draft that increases with shroud cross sectional area and shroud length. Very large particles that show reduced plume-like behavior may not be as efficient in inducing draft, but they will still induce at least half of the theoretical flow.

ACKNOWLEDGMENTS

This work was supported by the Ocean Carbon Sequestration Program, Biological and Environmental Research (BER), U.S. Dept. of Energy (grant number DE-FG02-01ER63078), the National Energy Technology Laboratory, U.S. Dept. of Energy (grant number DE-FG26-98FT40334) and the Martin Family Fellows for Sustainability. From Oak Ridge National Laboratory (ORNL), Dr. Costas Tsouris, Scott McCallum, David Riestenberg and Phil Szymcek developed and performed laboratory scale experiments on the hydrate injector. Drs. Peter Brewer, Ed Peltzer, Peter Walz and members of the Monterey Bay Aquarium Research Institute (MBARI) provided time and expertise on the research vessel Western Flyer during the field studies that motivated the paper. At MIT, Shannon O'Connell and Emily Moberg provided help with the laboratory experiments.

REFERENCES

- [1] Intergovernmental Panel on Climate Change (IPCC) (2005) Special report on carbon dioxide capture and storage, B. Metz, O. Davidson, H. C. de Coninck, M. Loos, and L. Meyer (ed) (Cambridge University Press, Cambridge, United Kingdom and New York, NY, USA
- [2] Sloan ED (1998) Gas hydrates: Review of physical/chemical properties. *Energy and Fuels* 12(2): 191-196
- [3] Lee S, Liang L, Riestenberg D, West OR, Tsouris C, Adams E (2003) CO₂ hydrate composite for ocean carbon sequestration. *Env Sci and Tech* 37:3701–3708
- [4] Tsouris C, Brewer P, Peltzer E, Walz P, Riestenberg D, Liang L, West O (2004) Hydrate composite particles for ocean carbon sequestration: field verification. *Env Sci and Tech* 38(8):2470–2475
- [5] Tsouris C, McCallum S, Aaron D, Reistenberg D, Gabitto J, Chow A, Adams E (2007) Scale-up of a continuous-jet hydrate reactor for CO₂ ocean sequestration. *AIChE Journal* 53(4):1017–1027
- [6] Tsouris C, Szymcek P, Taboada-Serrano P, McCallum SD, Brewer P, Peltzer E, Walz P, Adams E, Chow A, Johnson WK, Summers J (2007) Scaled-up ocean injection of CO₂-hydrate composite particles. *Energy and Fuels* 21:3300–3309
- [7] Riestenberg DE, Tsouris C, Brewer PG, Peltzer ET, Walz P, Chow AC, Adams EE (2005) Field studies on the formation of sinking CO₂ particles for ocean carbon sequestration: Effects of injector geometry on particle density and dissolution rate and model simulation of plume behavior. *Env Sci and Tech* 39(18):7287 – 7293
- [8] Chow A (2008) Fluid dynamics of sinking carbon dioxide hydrate particle releases for direct ocean carbon sequestration. Dissertation, Dept. Civil and Environmental Engineering, Massachusetts Institute of Technology
- [9] Israelsson PH, Chow AC, Adams EE (2010) An updated assessment of the acute impacts of ocean carbon sequestration by direct injection. *Int J Greenhouse Gas Control* 4: 262-271
- [10] Wannamaker EJ, Adams EE (2006) Modeling descending carbon dioxide injections in the ocean. *J Hydraul Res* 44(3):324–337
- [11] Crounse B, Wannamaker EJ, Adams EE (2007) Integral model of a multiphase plume in quiescent stratification. *J Hydraul Eng* 133(1)
- [12] Chow AC, Adams EE, Israelsson PH, Tsouris C (2008) Carbon dioxide hydrate particles for ocean carbon sequestration. *Greenhouse Gas Control Technologies* 9. Book Series: Energy Procedia, 1:4937-4944, 2009.
- [13] Schlitzer R (2000) Electronic atlas of WOCE hydrographic and tracer data now available <http://www.ewoce.org>. *Eos Trans. AGU*, 81(5):45
- [14] S. A. Socolofsky and E. E. Adams. Multi-phase plumes in uniform and stratified crossflow. *J. Hydraulic Research*, 40(6):661–672, 2002.

- [15] Silvester R (1967) Jet mixers in sewage outfalls. *J Inst Eng Australia*, 33–37.
- [16] Argaman Y, Vajda M, Galil N (1975) Use of jet pumps in marine waste disposal. *J. Env Eng Div ASCE* 101(E5):703–711
- [17] Adams E (1982) Dilution analysis for unidirectional diffusers. *J Hydraul Div ASCE* 108(HY3):327–342
- [18] Parr D, Melville JG (1981) Near field performance of river diffusers. *J Env Eng Div ASCE* 107(E5):995–1008
- [19] Cheremisinoff NP (1981) *Cooling towers: selection, design, and practice*. Ann Arbor Science Publishers
- [20] Govier G, Radford B, Dunn J (1957) The upward vertical flow of air water mixtures: I. effect of air and water-rates on flow pattern, holdup and pressure drop. *Canadian J Chem Eng*, 35:58–70
- [21] Kajishima T, Saito T, Nagaosa R, Hatano H (1995) A gas-lift system for CO₂ release into shallow seawater. *Energy Convers Manag* 36(6-9):467–470
- [22] Adams EE, Golomb D, Zhang XY, Herzog HJ (1995) Confined release of CO₂ into shallow sea water. In: *Direct Ocean Disposal of Carbon Dioxide*, TERRAPUB, Tokyo, pp 153-164
- [23] Mays L (ed) (1999) *Hydraulic design handbook*. McGraw-Hill, New York
- [24] Wilkinson DL (1988) Avoidance of seawater intrusion into ports of ocean outfalls. *J. Hydr. Engrg* 114:218-228.
- [25] Fischer HB, List EJ, Koh RCY, Imberger J (1979) *Mixing in Inland and Coastal Waters*. Academic Press
- [26] Milgram JH (1983) Mean flow in round bubble plumes. *J Fluid Mech* 133:345–376
- [27] Asaeda T, Imberger J (1993) Structure of bubble plumes in linearly stratified environments. *J Fluid Mech* 249:35–57
- [28] Crabtree BJ, Bridgwater JR (1971) Bubble coalescence in viscous liquids. *Chem Eng Sci* 26:839–851
- [29] Tsuchiya K, Miyahara T, Fan L (1989) Visualization of bubble-wake interactions for a stream of bubbles in a two-dimensional liquid-solid fluidized bed. *Int J Multiphase Flow* 15:35–49
- [30] Stewart C (1995) Bubble interaction in low-viscosity liquids. *Int J Multiphase Flow*, 21:1037–1046
- [31] Otake T, Tone S, Nakao K, Mitsuhashi Y (1977) Coalescence and breakup of bubbles in liquids. *Chem Eng Sci* 32:377–383
- [32] Lazarek GM, Littman H (1974) The pressure field due to a large circular capped air bubble rising in water. *J Fluid Mech* 66(4):673–687

- [33] Dietrich W (1982) Settling velocity of natural particles. *Water Resources Res* 18(6):1615–1626
- [34] Gui L, Merzkirch W (2000) A comparative study of the MQD method and several correlation-based PIV evaluation algorithms. *Exp in Fluids* 28(1):36–44
- [35] Dickson AG, Goyet C (1994) Handbook of methods for the analysis of the various parameters of the carbon dioxide system in sea water (version 2). Technical report ORNL/CDIAC-74, US Department of Energy
- [36] Weiss RF (1974) Carbon dioxide in water and seawater: the solubility of a non-ideal gas. *Mar Chem* 2:203-215
- [37] Volk T, Hoffert MI (1985). Ocean carbon pumps: analysis of relative strengths and efficiencies in ocean-driven atmospheric CO₂ changes. In: Sundquist ET, Broecker WS (eds), *Geophysical monograph 32, The carbon cycle and atmospheric CO₂: natural variations archean to present*, American Geophysical Union, 99–110

FIGURE CAPTIONS

Fig. 1 Schematic of shrouded release (inverted chimney). Left: isolated plume affected by ambient current and stratification. Right: after - plume released in shroud, creating a down draft Q .

Fig. 2 Theoretical induced flow rates versus shroud aspect ratio. Flows are normalized by $Q_{\text{theo}} = (BA^2h)^{1/3}$, the idealized flow rate for a frictionless shroud with distributed single phase buoyancy source. Q_c is flow rate from a centralized single phase buoyancy source with no shroud friction; Q_f is flow from a centralized single phase buoyancy source with two friction factors, $f=0.03$ and 0.055 ; Q_λ is the flow rate from a centralized source, including friction ($f=0.055$), and accounting for reduced plume spreading with $\lambda=0.5$. Q_{free} is the free (unshrouded) plume flow rate evaluated at depth h .

Fig. 3 Release mechanisms for beads shown with laser light source and suspended shroud in center. Release mechanism for brine (left) and balls (right).

Fig. 4 Buoyant releases in a shroud of aspect ratio $h/d = 2$ (top), $h/d = 4$ (middle) and $h/d = 10$ (bottom). Each release is of comparable initial kinematic buoyancy flux B . Left: dyed brine release; center: glass bead release; right: high density ball release.

Fig. 5 Example steady state flow field calculated by PIV above shroud. Pipe radius $R_0 = 1.2$ cm, Shroud radius $R=d/2=15$ cm, Shroud height $h=91$ cm. Coordinate axis defined by arrows shown (positive h upwards, positive r away from shroud center). A control volume used to measure the inflow into a shroud is also shown.

Fig. 6 Plot of the time series of the downward velocity at four points at the height of the lip of the shroud for one experiment, showing the ramping up of downward velocities as the siphon effect builds up after the start of the continuous particle release at time=0 seconds. Steady state was attained after about 31 s.

Fig. 7 Experimentally measured shroud flows normalized by $Q_{\text{theo}} = (BA^2h)^{1/3}$, as a function of shroud aspect ratio h/d , superimposed onto theoretical results of Figure 2. Typical standard deviations for multiple measurements of Q are shown as vertical error bars.

Fig. 8 Experimentally measured shroud flows normalized by $Q_{\text{theo}} = (BA^2h)^{1/3}$, as a function of the dimensionless slip velocity u_s/u_{theo} . Results are from experiments with a shroud aspect ratio $h/d=10$. Typical error bars for both the normalized slip velocity (horizontal) and the normalized induced flow rates (vertical) are shown.

Fig. 9 Predicted shroud flow Q as a function of aspect ratio, for a shroud efficiency of $Q/Q_{\text{theo}}=0.6$. Initial hydrate release is 100 kg/s of CO_2 , with hydrate particle densities of 1.04 g/cm^3 from a centralized source. The predicted flows do not hold for $h/d < 1$ because the shroud does not flow full.

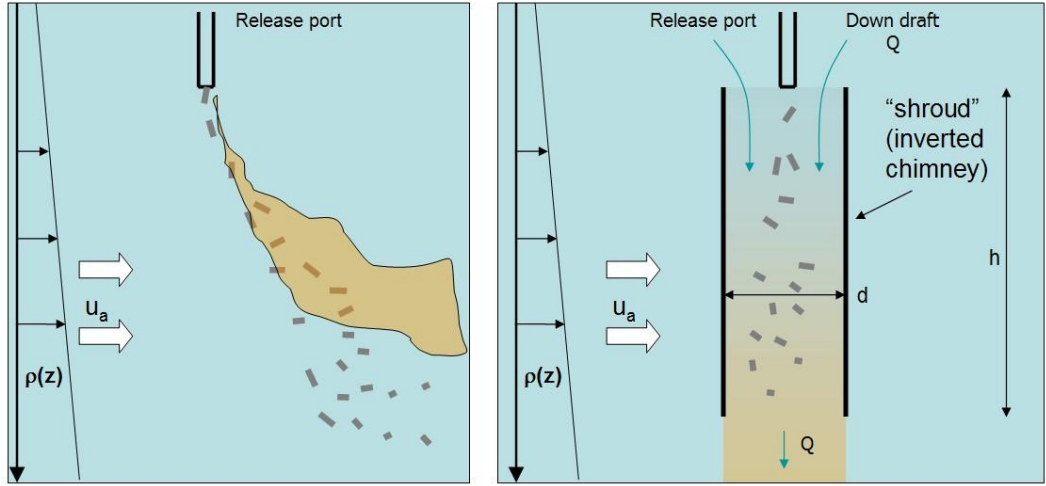


Fig. 1 Schematic of shrouded release (inverted chimney). Left: isolated plume affected by ambient current and stratification. Right: after - plume released in shroud, creating a down draft Q .

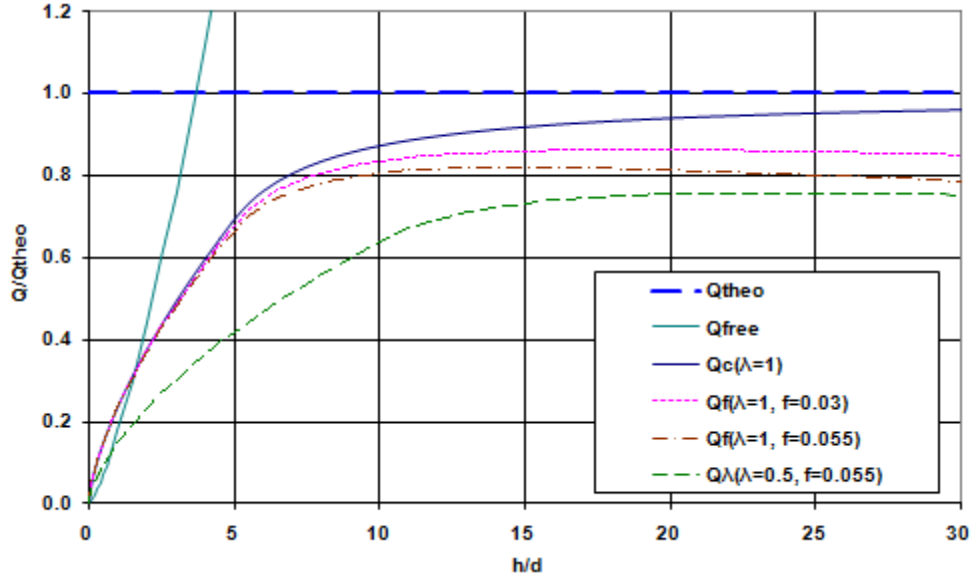


Fig. 2 Theoretical induced flow rates versus shroud aspect ratio. Flows are normalized by $Q_{theo} = (BA^2h)^{1/3}$, the idealized flow rate for a frictionless shroud with distributed single phase buoyancy source. Q_c is flow rate from a centralized single phase buoyancy source with no shroud friction; Q_f is flow from a centralized single phase buoyancy source with two friction factors, $f=0.03$ and 0.055 ; Q_λ is the flow rate from a centralized source, including friction ($f=0.055$), and accounting for reduced plume spreading with $\lambda=0.5$. Q_{free} is the free (unshrouded) plume flow rate evaluated at depth h .

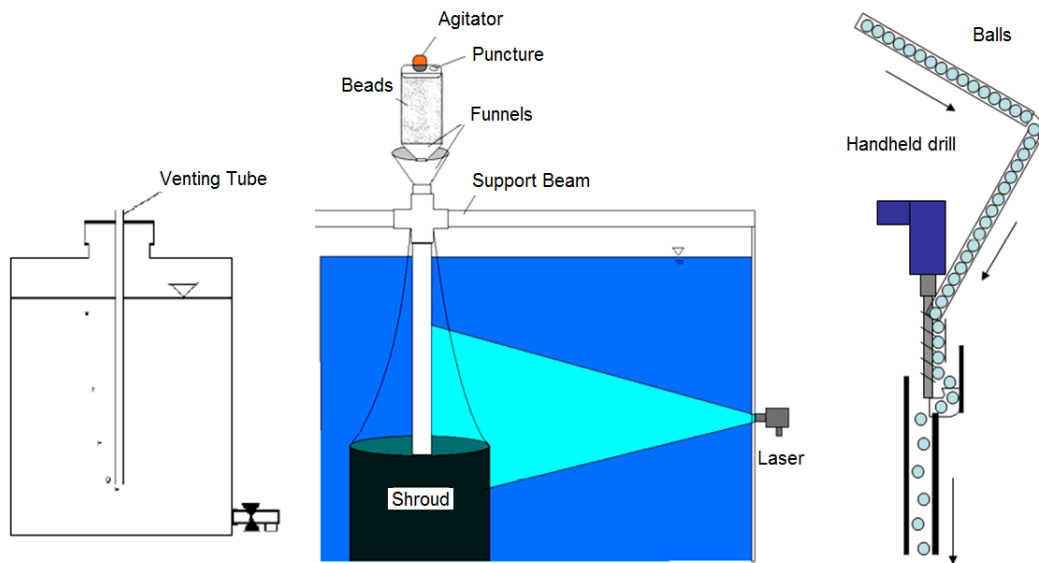


Fig. 3 Release mechanisms for beads shown with laser light source and suspended shroud in center. Release mechanism for brine (left) and balls (right).

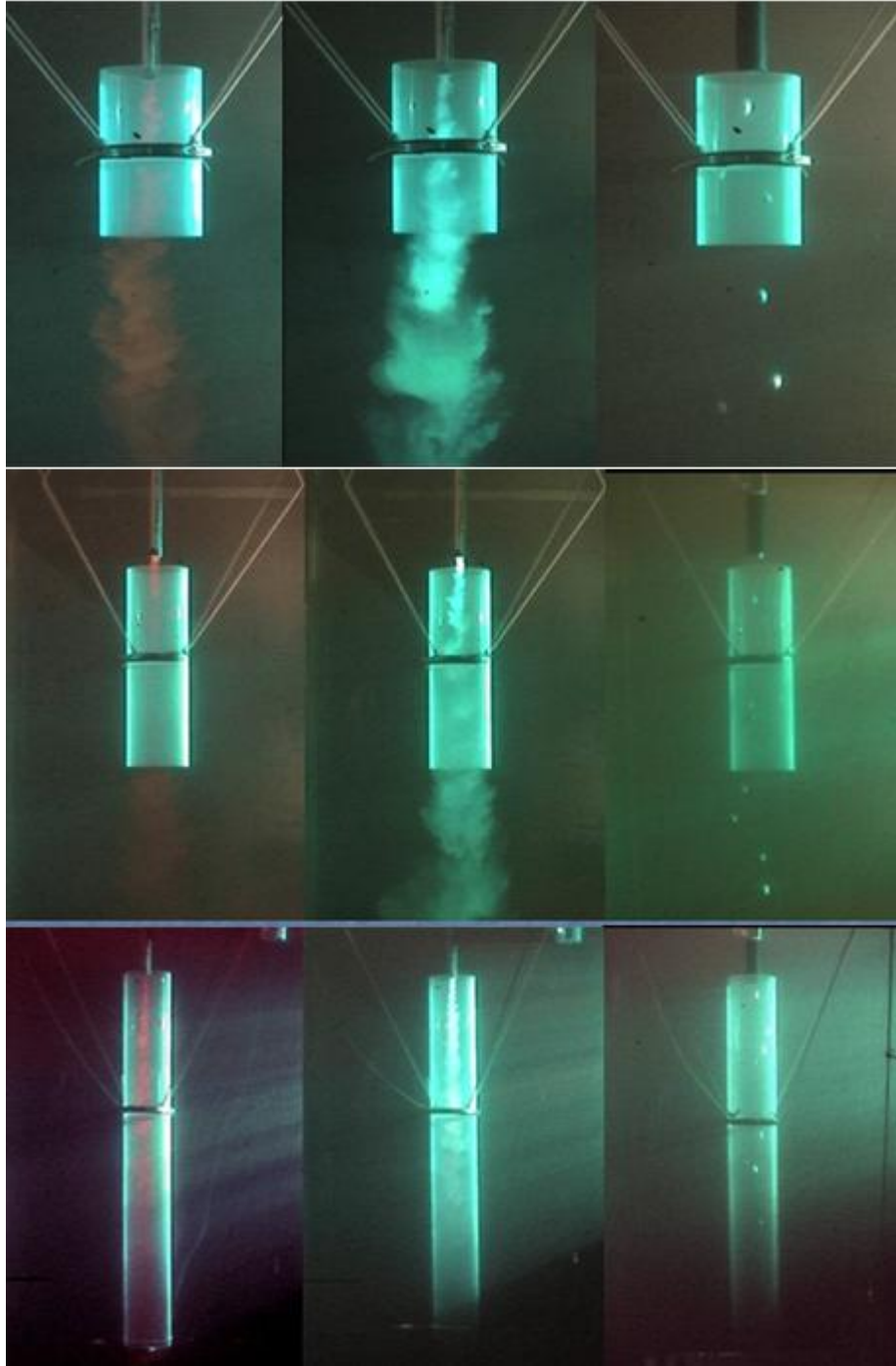


Fig. 4 Buoyant releases in a shroud of aspect ratio $h/d = 2$ (top), $h/d = 4$ (middle) and $h/d = 10$ (bottom). Each release is of comparable initial kinematic buoyancy flux B . Left: dyed brine release; center: glass bead release; right: high density ball release.

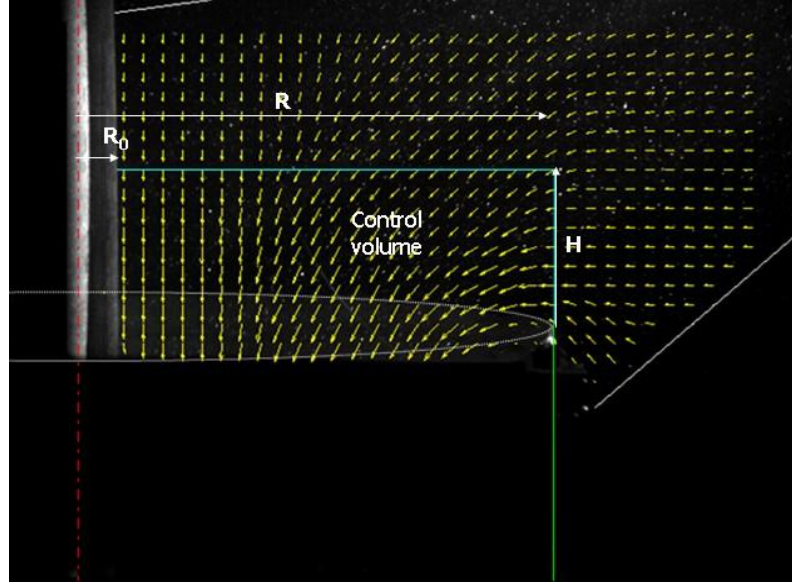


Fig. 5 Example steady state flow field calculated by PIV above shroud. Pipe radius $R_0 = 1.2$ cm, Shroud radius $R=d/2=15$ cm, Shroud height $h=91$ cm. Coordinate axis defined by arrows shown (positive h upwards, positive r away from shroud center). A control volume used to measure the inflow into a shroud is also shown.

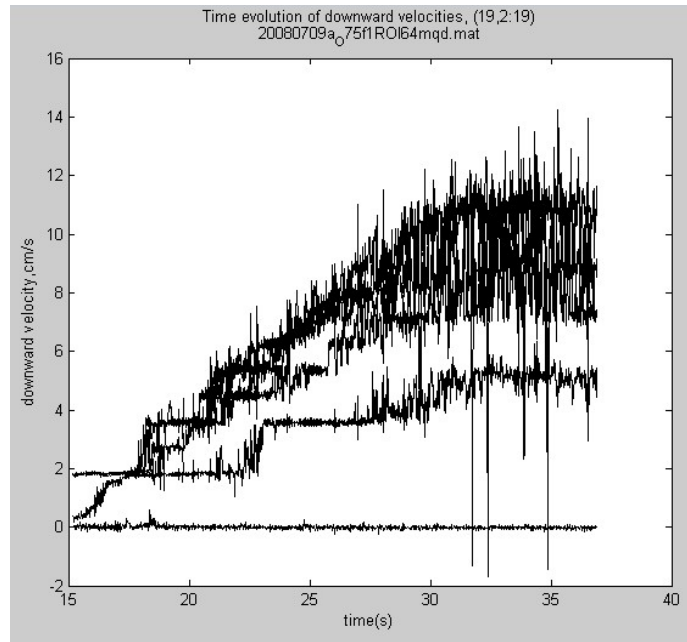


Fig. 6 Plot of the time series of the downward velocity at four points at the height of the lip of the shroud for one experiment, showing the ramping up of downward velocities as the siphon effect builds up after the start of the continuous particle release at time=0 seconds. Steady state was attained after about 31 s.

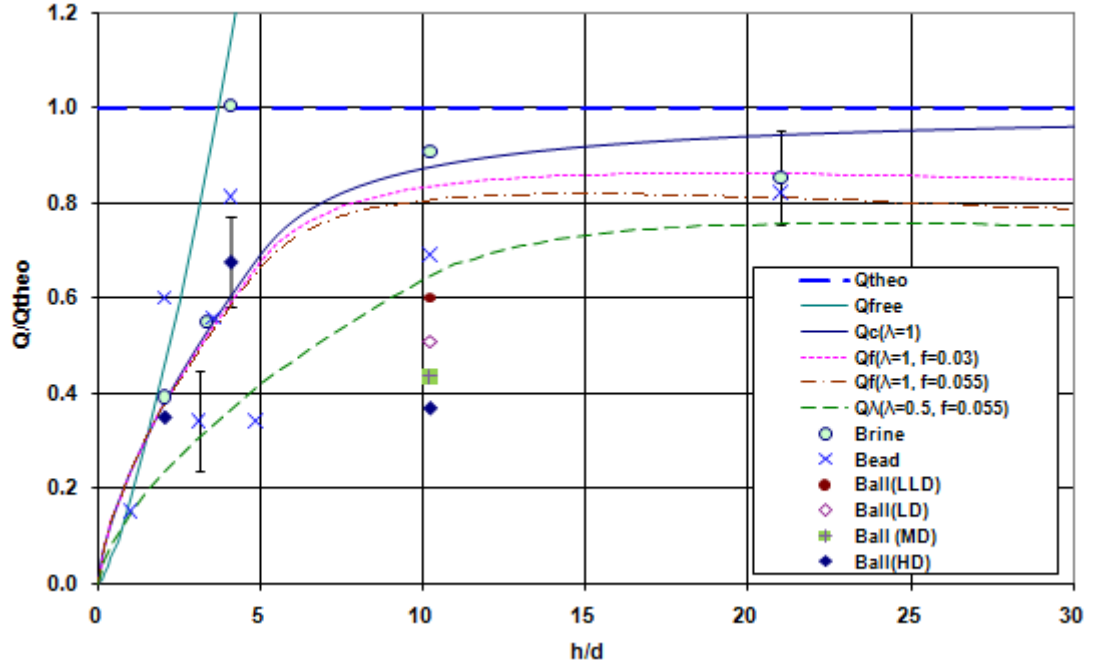


Fig. 7 Experimentally measured shroud flows normalized by $Q_{\text{theo}} = (BA^2h)^{1/3}$, as a function of shroud aspect ratio h/d , superimposed onto theoretical results of Figure 2. Typical standard deviations for multiple measurements of Q are shown as vertical error bars.

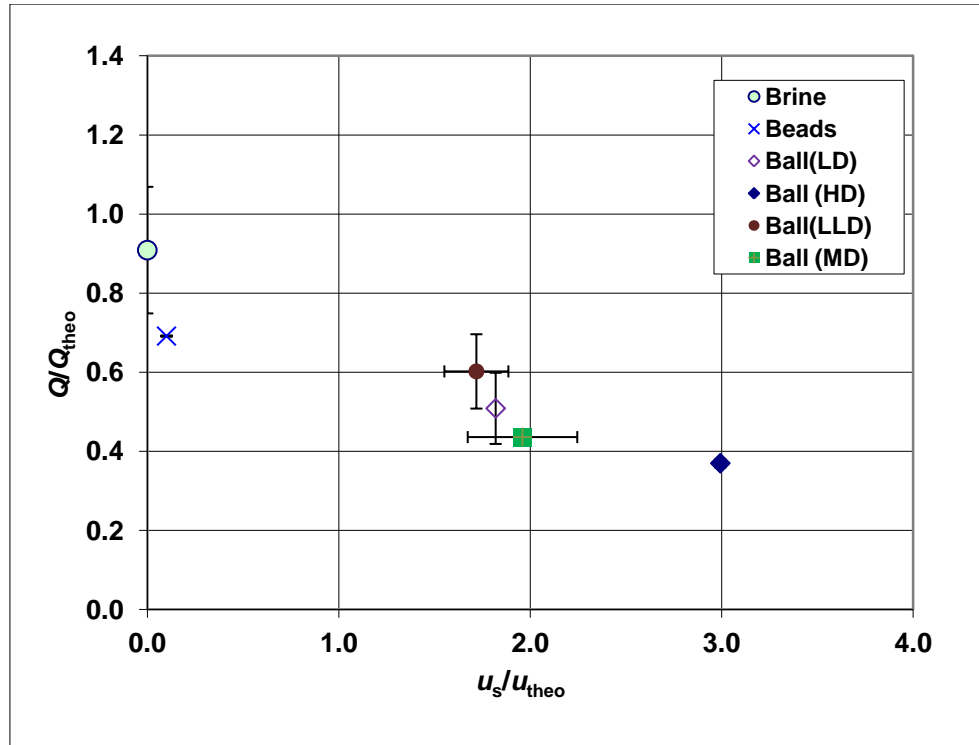


Fig. 8 Experimentally measured shroud flows normalized by $Q_{theo} = (BA^2h)^{1/3}$, as a function of the dimensionless slip velocity u_s/u_{theo} . Results are from experiments with a shroud aspect ratio $h/d=10$. Typical error bars for both the normalized slip velocity (horizontal) and the normalized induced flow rates (vertical) are shown.

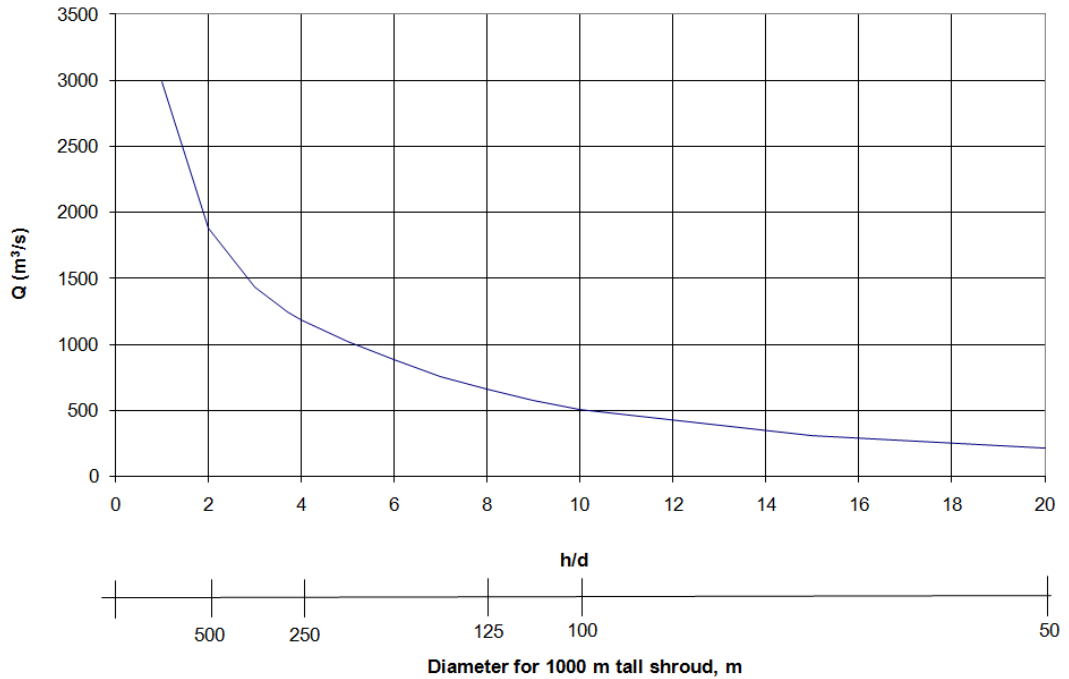


Fig. 9 Predicted shroud flow Q as a function of aspect ratio, for a shroud efficiency of $Q/Q_{theo}=0.6$. Initial hydrate release is 100 kg/s of CO_2 , with hydrate particle densities of 1.04 g/cm^3 from a centralized source. The predicted flows do not hold for $h/d < 1$ because the shroud does not flow full.